

# Near-field Raman imaging of morphological and chemical defects in organic crystals with subdiffraction resolution

P. G. GUCCIARDI\*, S. TRUSSO\*, C. VASI\*, S. PATANÈ† & M. ALLEGRINI‡

\*CNR- Istituto per i Processi Chimico-Fisici, sez. Messina, Via La Farina 237, I-98123 Messina, Italy

†Dipartimento di Fisica della Materia e Tecnologie Fisiche Avanzate, INFN, Università di Messina, Salita Sperone 37, I-98166 Messina, Italy

‡INFN, Dipartimento Fisica Università di Pisa, Via Buonarroti, 2, I-56127 Pisa, Italy

**Key words.** Near-field, organic crystals, Raman spectroscopy.

## Summary

In this study we report on the application of an aperture near-field optical microscope for Raman imaging of organic materials. Spectral analysis and detailed Raman imaging are performed with integration times of 100 ms per point, without the aid of field enhancement effects. The studied samples consist of two high Raman-efficiency molecular samples: a 7,7',8,8'-tetracyanoquinodimethane crystal showing surface defects and a 7,7',8,8'-tetracyanoquinodimethane thin film characterized by the presence of submicrometre-sized organo-metallic copper-salt complexes. In the first case, the effect of the surface deformation was studied, whereas in the second sample we were able to chemically image the formation of salt complexes. Subdiffraction resolution was achieved in both studies.

## Introduction

Spectral contrast has given a tremendous momentum to near-field scanning optical microscopy (NSOM) (Lewis *et al.*, 1984; Pohl *et al.*, 1984) for materials science investigations at the nanometre scale. The combination of NSOM techniques and Raman spectroscopy represents an important improvement towards materials phase analysis, chemical recognition and local stress measurements at scales beyond the diffraction limit ( $\approx 230$  nm using green light and immersion oil microscope objectives). Near-field Raman spectroscopy using optical fibre probes as sensors (Betzig *et al.*, 1991) is challenging for two main reasons: first, Raman scattering is an extremely inefficient process ( $\approx 14$  orders of magnitude smaller with respect to fluorescent dyes); second, the maximum amount of

light available for illumination mode NSOM experiments is limited to  $\approx 1$   $\mu$ W because of the low throughput of the metalized NSOM probes ( $10^{-4}$  for 100-nm diameter apertures), and the fact that thermal damages arise when laser powers  $> \approx 10$  mW are coupled to the NSOM fibres.

Early NSOM-Raman experiments aimed at demonstrating the feasibility of this new technique. The first spectra were reported by Tsai *et al.* (1994) on diamond particles, and pioneering work in near-field Raman imaging was carried out by the groups of Hallen and Batchelder. Hallen and colleagues were able to carry out submicrometre resolution NSOM-Raman maps of rubidium-doped zones in  $\text{KTiOPO}_4$  crystals (Jahncke *et al.*, 1995, 1996) and, subsequently, to provide evidence of the different selection rules holding in far- and near-field Raman spectroscopy (Ayars *et al.*, 2000). The latter group was able to detect the weak Raman signal of silicon (Smith *et al.*, 1995), demonstrating the possibility of carrying out stress distribution maps using NSOM means, with submicrometre resolution (Webster *et al.*, 1998). Diffraction limited (submicrometre) resolution was reported in both experiments performed using pulled, metal-coated fibre probes to excite the sample (illumination mode), while detecting the backscattered light through long working-distance microscope objectives. A spectral resolution  $> 10$   $\text{cm}^{-1}$  was reported and very long integration times ( $\approx 10$  h) were required to map of a few tens of points per line. The exploitation of resonant Raman enhancement (Smith *et al.*, 1995), or the use of surface-enhanced Raman scattering (SERS) effects turned out to be an effective way of obtaining NSOM-Raman data with higher signal-to-noise ratios and reasonable exposure times. For instance, Emory & Nie (1997) and Zenobi's group (Ziesel *et al.*, 1998; Stöckle *et al.*, 2000) reported NSOM-Raman spectra of rhodamine 6G absorbed on silver nanoparticle-rich substrates (so-called SERS-active substrates), demonstrating enhancement factors of the order of  $10^{13}$ . Subsequently, dye-labelled

Correspondence to: P. G. Gucciardi. Tel.: +39 90 293 9693; fax: +39 90 293 9902; e-mail: gucciardi@me.cnr.it

DNA molecules deposited on SERS-active substrates were imaged with 100 nm spatial resolution (integration time: 60 s per point-spectrum) by Deckert *et al.* (1998) using high-throughput NSOM fibre probes (Stöckle *et al.*, 1999). The need to deposit the sample on SERS-active substrates, however, severely limits the applications of this technique. New apertureless-NSOM configurations, using metallized atomic force microscopy tips to locally enhance the excitation field, were thus introduced by Stöckle *et al.* (1999), and Hayazawa *et al.* (2000, 2001) (in combination with SERS active substrates). In both experiments a very thin sample layer was deposited onto a transparent substrate and illuminated from below through an immersion oil objective. The backscattered Raman signal was gathered through the same objective, whereas the tip was raster scanned on top of the surface. Enhancement factors of the order of  $10^3$  were reported, respectively, in brilliant cresyl blue and rhodamine molecules, and spectral inhomogeneity was found to arise at lateral scales of 55 nm (integration time: 60 s) and 30 nm (integration time: 1 s), respectively. More recently, Futamata & Bruckbauer, (2001) demonstrated the possibility of combining SERS effects with Raman-photon scanning tunnelling microscopy, yielding Raman spectra of copper phthalocyanine with integration times of only 2 s.

Here, we show the applications of an aperture-NSOM Raman set-up to image the morphological and chemical properties of a class of high Raman efficiency organic materials. Raman imaging with subdiffraction resolution is reported without field enhancement effects exploitation, and using very short integration times.

## Materials and methods

### Experimental set-up

A detailed description of the home-made set-up can be found in Gucciardi *et al.* (1997, 2002). For the reported experiments we worked in the illumination mode (Fig. 1) and adopted the reflection configuration, this being the most versatile for materials investigations. Commercially available fibre probes (Nanonics Ltd) with a nominal aperture of 100 nm were used, coupled to an argon ion laser delivering up to 100 mW of continuous power at 514.5 nm. In order to preserve the metal coating integrity, no more than 10 mW were coupled to the probe, yielding a far-field output power ranging between 10 and 100 nW, depending on both the actual aperture diameter and the apical cone angle. The fibre was glued to a quartz tuning-fork exploited for nonoptical shear-force detection (Betzig *et al.*, 1992; Toledo-Crow *et al.*, 1992; Karrai & Grober, 1995). The sample was scanned by means of a piezo-cylinder and the backscattered light collected using a high numerical aperture ( $NA = 0.51$ ), long working distance (10.6 mm) microscope objective resting at  $45^\circ$  with respect to the probe axis. The light was thus coupled to a multimode optical fibre and driven

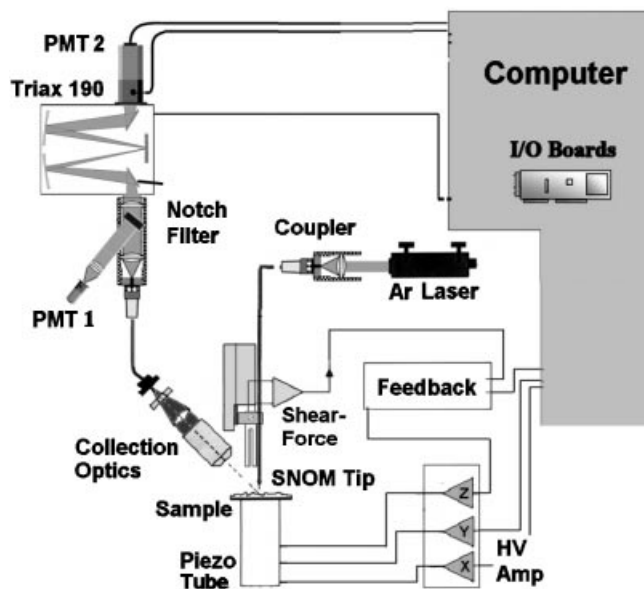


Fig. 1. Sketch of the NSOM-Raman set-up. PMT: photomultiplier, Triax 190: Monochromator.

to the monochromator. A notch filter (rejection ratio  $\approx 10^6$ ), placed between the two lenses matching the  $F$ -numbers of the fibre and the monochromator, reflected back the laser light to a photomultiplier (PMT1), providing the elastic scattering signal. A single grating ( $1200 \text{ lines mm}^{-1}$ ), 190 mm focal length monochromator was preferred, because of the high luminosity in spite of a lower spectral resolution (nominal resolution 0.3 nm). The Raman signal was thus detected by a further photomultiplier (PMT2) working in photon-counting mode, simultaneous to the topography and the elastic scattering. The apparatus is very compact and stable, thus no appreciable drifts were observed among subsequent scans. The system is driven by a software written in Visual Basic, using advanced object-orientated programming techniques.

### Materials

Materials based on 7,7',8,8'-tetracyanoquinodimethane (TCNQ) and its organometallic compounds have been proposed for applications in molecular electronic devices such as switches (Gao & Kahn, 2001), organic light-emitting devices (Blochwitz *et al.*, 1998) and data storage media (Hua & Chen, 1992). TCNQ is a strong electron acceptor and forms a variety of charge-transfer (CT) complexes with inorganic and organic donors. The molecular CT complex formed by the interaction of a donor (D) and an acceptor (A) can be considered as a resonance hybrid of two structures: one, a no-bond structure (D, A) in which the two species are bound together by van der Waal's forces, and the other ionic structure ( $D^+$ ,  $A^-$ ) in which the two structures are bound by a covalent bond (Graja,

1997). These complexes are characterized by the occurrence of strong absorption bands in the near-infrared and in the visible spectrum, depending on the degree of charge transfer  $\rho$ . If  $\rho = 1$  then the system contains only  $A^-$  ions, whereas if  $0 < \rho < 1$  then both  $A^-$  and  $A^0$  species exist.

Copper complexes of TCNQ, in particular, exhibit unique electrical and optical field-induced switching and memory phenomena. The resistivity of CuTCNQ complex films coated with Al, in fact, switches from a high to a low impedance state under the application of an external electric field or laser irradiation. Because the properties of these molecular semiconductors vary greatly with crystallographic orientation, degree of crystallinity and the chemical composition of the films, a valuable contribution to a detailed understanding of the morphology, spectroscopy and chemistry of these materials in bulk, in thin films and at interfaces can be given by scanning probe techniques, such as atomic force and scanning tunnelling microscopy (Higo *et al.*, 2001 and references therein).

TCNQ-based complexes are suitable for NSOM investigations for two reasons: first, the high Raman efficiency of the material makes it suitable for experiments with low excitation powers; second, because in the TCNQ CT complexes the electron-phonon coupling provokes both a decrease of the Raman activity and a shift of the vibration frequencies, thus yielding a valuable source of chemical contrast.

The first investigated sample (sample A) is a TCNQ single crystal grown by precipitation from solution. A first inspection using conventional microscopy allowed us to show the flat crystallographic surfaces, some of which showed surface damages.

The second sample (sample B) is a TCNQ thin film grown by means of a thermal ultra-high-vacuum deposition process starting by TCNQ powder. The organic thin film, of  $t \approx 1 \mu\text{m}$  thick, has been grown onto a potassium bromide single crystal substrate. To be sure of the good quality of the film, we performed infrared transmission measurements using a

Perkin-Elmer IR 330 spectrometer. The results clearly showed all of the typical infrared peaks of TCNQ, indicating that molecular integrity was preserved during the deposition, and that the film was in a completely amorphous state. The sample was thus covered with a fine copper powder and stored at  $40^\circ\text{C}$  for about one month. After this period the yellow surface of the sample began to be populated with a number of blue spots indicating the presence of the typical CuTCNQ complexes.

## Results and discussion

Figure 2(a) shows the geometry of the TCNQ molecule. The normal coordinates related to the eigenmodes of the four most intense vibrations at  $1207$ ,  $1453$ ,  $1602$  and  $2230 \text{ cm}^{-1}$  are highlighted by arrows. The energy values are reproduced by the sharp peaks in the Raman spectra of Fig. 2(b), carried out by NSOM means in far-field (red line) and near-field (black line) illumination conditions, corresponding to probe-sample distances of  $\approx 4 \mu\text{m}$  and  $10 \text{ nm}$ , respectively. The integration time ( $\tau_{\text{INT}}$ ) was set to  $100 \text{ ms}$  per point, and a signal-to-noise ratio  $> 10$  was achieved. The  $1453 \text{ cm}^{-1}$  vibration appears as the most intense, in agreement with the literature, and thus represents the best candidate for imaging purposes. The large band occurring in the  $200\text{--}700 \text{ cm}^{-1}$  zone is due to the Raman emission of the silica fibre probe coming out from the edge aperture. The occurrence of this band, first reported by Grausem *et al.* (1997), represents a further difficulty for applications to materials with Raman activity in this spectral range such as silicon or other semiconductor materials. The intensity decrease of both the Rayleigh tail and the silica Raman emission, observed when approaching the probe to the sample surface, are due to shadowing effects.

The surface properties of sample A have thus been studied. In Fig. 3 we show the topography (Fig. 3a) and the Raman map (Fig. 3b) at  $1453 \text{ cm}^{-1}$  on an area  $15 \times 15 \mu\text{m}^2$  wide. The maps consist of  $128 \times 128$  points. Setting  $\tau_{\text{INT}} = 100 \text{ ms}$ , leads

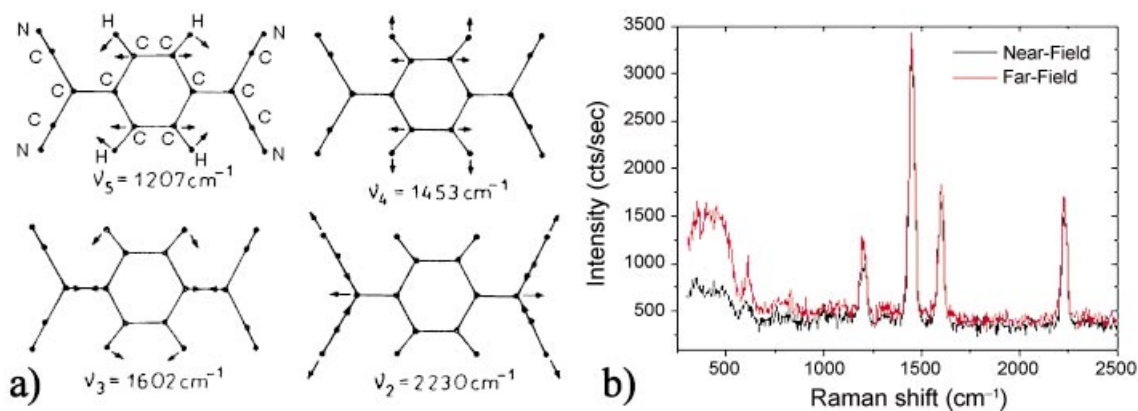
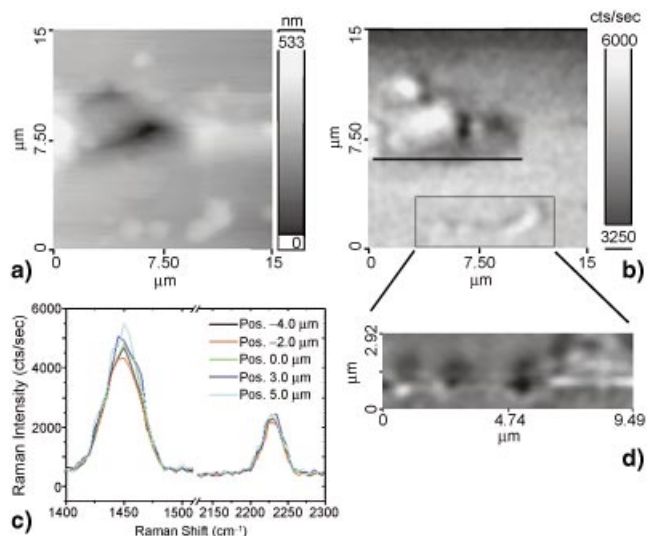
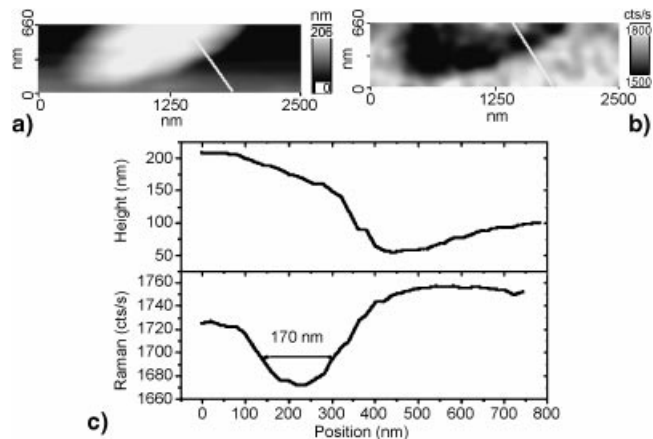


Fig. 2. (a) Chemical structure of the TCNQ. The normal modes of the four most intense normal modes are highlighted by the arrows. (b) Raman spectra of TCNQ acquired in near-field (black line, tip-sample distance  $\approx 10 \text{ nm}$ ) and far-field (red line, tip-sample distance  $\approx 4 \mu\text{m}$ ) illumination conditions.



**Fig. 3.** Topography (a) and Raman scattering map (b) of the TCNQ crystal carried out at  $1453\text{ cm}^{-1}$ . (c) Raman spectra collected along the line drawn in (b) at a distance of  $2\text{ }\mu\text{m}$ , showing fluctuations of the Raman intensity superimposed to a constant background. The rectangle in (b) indicates the location where the elastic scattering map (d) has been acquired.

to an overall acquisition time of  $< 1\text{ h}$ . The topography shows a rather flat surface with local corrugations. Two elongated holes, a few hundred nanometres deep, can be located in the central part of the figure and are probably due to scratches. Different bump-like features appear at the borders of the figure, with heights ranging from  $100\text{ nm}$  (those located on top and at the bottom of the image) to  $500\text{ nm}$  (on the left-hand side). As opposed to the scratches, these structures are more likely due to defects that occurred during the growth process. The corresponding Raman map is very rich of detail. In particular, the topography features always produce a modulation of the Raman activity, whose pattern, however, is different from the topography one. The bump-like structures, in particular, are always surrounded by a zone of depleted Raman intensity by  $10\text{--}20\%$ , whereas at their centre the Raman activity increases by  $5\text{--}25\%$  with respect to the flat area. In order to obtain a spectral insight into this behaviour, we carried out several Raman spectra along the black line indicated in Fig. 3(b), some of which are reported in Fig. 3(c). Only the peaks at  $1453$  and  $2230\text{ cm}^{-1}$  are shown, for clarity. Within our spectral resolution ( $30\text{ cm}^{-1}$ ) no clear shift of the peaks can be appreciated, only a variation in the intensity maxima. We note that, although the Raman intensity varies as a function of the position, the background level is almost unchanged, showing very good rejection of the elastic scattered light. This is a key issue as spurious laser light, influencing the background level, could induce fictitious cross-talks (artefacts) between the elastic scattering and Raman signal.



**Fig. 4.** Topography (a) and Raman map (b) carried out at  $1602\text{ cm}^{-1}$  in correspondence of a surface defect of the TCNQ crystal. The line profiles (c) allow us to establish a feature height (upper) of  $150\text{ nm}$  and that, inside a contour  $\approx 170\text{ nm}$  large, the Raman activity (lower) is depleted with respect to the surrounding surface.

Geometrical artefacts, such as optical signal shadowing induced by topography structures, can be easily identified by comparing the Raman and elastic scattering maps, as they would be affected in a similar way. Thus, the different spatial pattern of the elastic scattering (Fig. 3D), with respect to the Raman one (rectangle in Fig. 3b), allows us to discard the hypothesis of geometrical artefacts producing the dark contours in the Raman image in correspondence of bumped structures.

A zoom ( $2.5 \times 0.66\text{ }\mu\text{m}^2$ ) on a zone showing a bump-like feature is reported in Fig. 4. The topography (Fig. 4a) shows a relief  $\approx 150\text{ nm}$  high (Fig. 4c, upper), whereas in the Raman map at  $1602\text{ cm}^{-1}$  (Fig. 4b) we can observe that a dark ring contours the relief. This behaviour is highlighted in the line profile displayed in Fig. 4(c, lower), which helps us in assessing an optical resolution of  $170\text{ nm}$  by using the full-width at half maximum (FWHM) criterion. The motivations of the observed Raman behaviour are indeed difficult to explain quantitatively. From a qualitative point of view, however, depletion of the Raman activity observed at the contour of the bumps could be explained by the occurrence of TCNQ in an amorphous state. Similarly, a different molecular organization at the level of microcrystalline clusters, or an increased material density, could account for the increase of the Raman signal in proximity of the bump apices or nearby the scratches.

Things are simpler for what concerns sample B in which the only source of contrast in Raman maps is provided by the presence of two different chemical species (TCNQ and CuTCNQ). In Fig. 5 we show a microphotograph  $500 \times 250\text{ }\mu\text{m}^2$  wide obtained using conventional microscopy under white light illumination. The 'yellow zone' consists of TCNQ molecules in the amorphous state, whereas the strong absorption bands

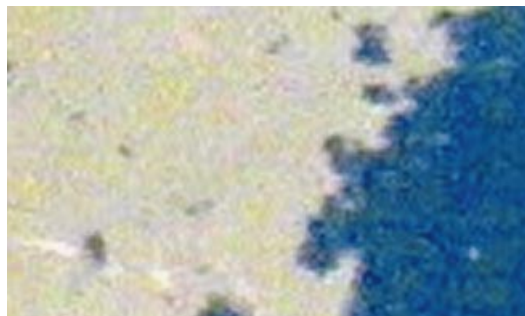


**Fig. 5.** Microphotograph  $500 \times 250 \mu\text{m}^2$  wide of sample B, showing several blue CuTCNQ zones occurring on the yellow TCNQ film surface.

related to the CuTCNQ formation (Graja, 1997) determine the colour of the 'blue zone'. As can be seen in Fig. 5, the two major areas are not homogeneous: in the yellow zone small blue CuTCNQ spots are visible, having dimensions ranging from several tens of micrometres to less than  $10 \mu\text{m}$ ; also, inside the blue zone on the right-hand side of the figure, several yellow TCNQ spots can be appreciated with dimensions in the micrometre range. This phenomenon, probably related to inhomogeneous copper powder coverage of the surface during the oxidation process, is studied in detail using NSOM below.

The first investigations were performed in the 'yellow zone' and the results are displayed in Fig. 6. The topography (Fig. 6a and  $10 \times 10 \mu\text{m}^2$ ,  $128 \times 128$  pts) appears rather corrugated, with reliefs  $\approx 300$  nm high showing up in the left upper corner. The elastic scattering image (Fig. 6b) shows several spot-like details, some of which (e.g. in correspondence of the surface reliefs) appear correlated with the topography, and could thus suffer from artefact contributions (Hecht *et al.*, 1997; Gucciardi & Colocci, 2001). Conversely, two darker areas appear, respectively, in the central left and bottom central part, which do not have any counterpart in the topography map. The Raman map at  $1453 \text{ cm}^{-1}$  (Fig. 6c,  $\tau_{\text{INT}} = 100$  ms) shows similar features (whose dimensions are in the micrometre range) with a depleted Raman activity. These zones could thus be attributed to the formation of CuTCNQ spots. In order to confirm this hypothesis, we carried out several spectra at different points, shown in Fig. 6(d). The lower plots ( $\tau_{\text{INT}} = 300$  ms) show that, moving from point to point, the Raman activity changes, and all the peaks show the same behaviour, superimposed on a constant background. When moving to the darkest areas, such as that located at the bottom of Fig. 6(c), a dramatic change in the Raman emission can be observed: first, overall intensity is reduced by more than one order of magnitude (an integration time of 5 s per point was necessary to achieve an acceptable signal-to-noise ratio); second, we can observe a shift of the  $1453 \text{ cm}^{-1}$  peak towards  $1380 \text{ cm}^{-1}$ , together with a reduction in the intensity ratio between the  $1453$  and  $1602 \text{ cm}^{-1}$  peaks, being the chemical fingerprint of the CuTCNQ occurrence (Liu *et al.*, 1996;

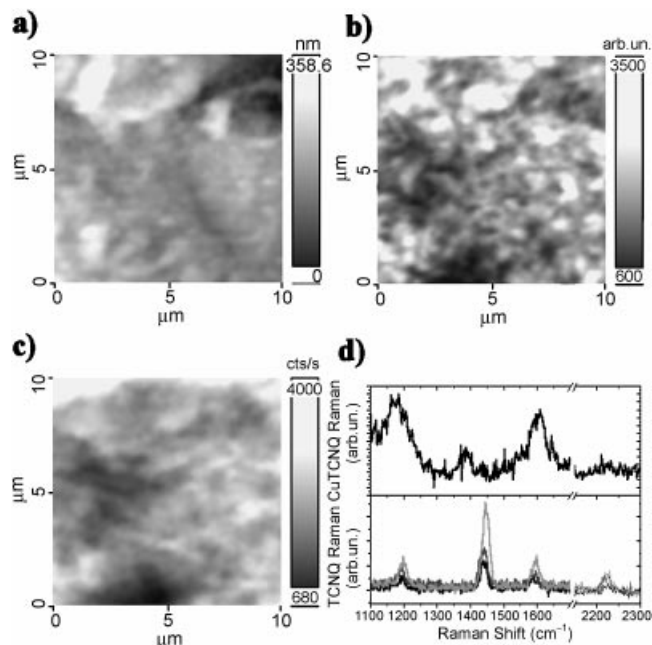


**Fig. 6.** Maps of the topography (a), elastic scattering (b), and Raman scattering at  $1453 \text{ cm}^{-1}$  (c) simultaneously acquired on sample B. The Raman spectra shown in d (lower) were collected at different points on a TCNQ-rich area with 300 ms of integration time. The Raman spectrum shown in d (upper) displays the shift of the  $1453 \text{ cm}^{-1}$  peak towards  $1381 \text{ cm}^{-1}$  as well as the strong decrease of the Raman activity (5 s integration time) typical of the CuTCNQ complex formation.

Gucciardi *et al.*, 2002). Several submicrometre spots showing a depleted or increased Raman emission are visible in the Raman map, showing that the chemical composition of the sample is not homogenous down to the nanometre scale. Thus, we zoomed in on an area  $2 \times 1.24 \mu\text{m}^2$ . Figure 7(a) shows the Raman map at  $1453 \text{ cm}^{-1}$  ( $\tau_{\text{INT}} = 100$  ms) and Fig. 7(b) the simultaneous elastic scattering image. Fluctuations of 25% in the Raman intensity can be appreciated on subwavelength scales, in particular, a spot of increased Raman activity with a FWHM  $\approx 150$  nm is visible in the upper right corner. The line profile of the Raman map (Fig. 7c, red circles) allows us to observe a spot of depleted intensity having a FWHM of 210 nm and to assess a step-like variation of the Raman signal of  $\approx 8\%$  within 175 nm (10–90% criterion). The different spatial behaviour of the elastic scattering profile (Fig. 7c, black diamonds), also visible in Fig. 6 in correspondence of several the submicrometre features, can be explained considering that the elastic scattering signal carries information not only about the local refractive index, but also contains contributions induced by the local geometry and by possible fictitious topography-related effects. The last two contributions can dominate the overall signal in those areas where absorption is not strong enough, producing new features in the elastic scattering map of non trivial interpretation.

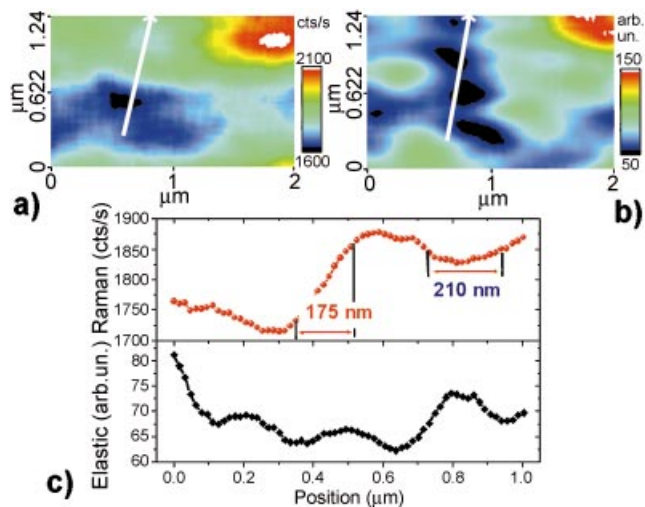


Fig. 7. (a) Raman map at  $1453\text{ cm}^{-1}$  and elastic-scattering image (b) simultaneously acquired on a TCNQ-rich zone. The Raman and elastic-scattering line profiles (lower and upper plot, respectively) reported in (c) refer to the line drawn in the maps.

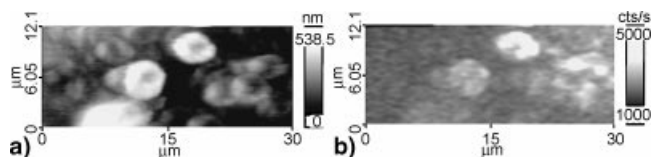


Fig. 8. Topography (a) and Raman map at  $1453\text{ cm}^{-1}$  (b) acquired on a CuTCNQ rich zone of sample B. The morphological and chemical behaviour in this area shows the formation of several doughnut-shaped structures, some of which contain neutral TCNQ (brighter zones in b).

Previous observations allow us to draw several conclusions regarding the chemical composition of sample B in the 'yellow zone': from both the Raman spectra and maps, we can deduce that TCNQ is the principal chemical compound in this area. The local decrease in Raman intensity is attributed to the occurrence of CuTCNQ spots having a thickness smaller than the near-field penetration depth, thus depleting the Raman signal of the TCNQ present underneath. Moreover, the small absorption taking place in such a thin CuTCNQ structure justifies the observed differences between the elastic and the Raman scattering maps. However, in some locations we are able to see deeper CuTCNQ structures, characterized by a much stronger light absorption, which produce a well visible contrast in the elastic scattering map, together with the vanishing of the Raman activity at  $1453\text{ cm}^{-1}$ , shifting towards  $1381\text{ cm}^{-1}$ .

A completely different morphology characterizes the 'blue' CuTCNQ zone. Figure 8 shows the topography (Fig. 8a) and Raman map at  $1453\text{ cm}^{-1}$  (Fig. 8b) of a  $30 \times 12.1\text{ }\mu\text{m}^2$

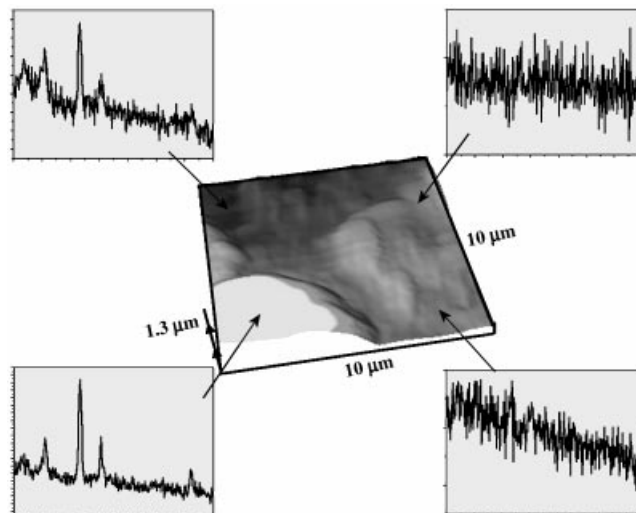
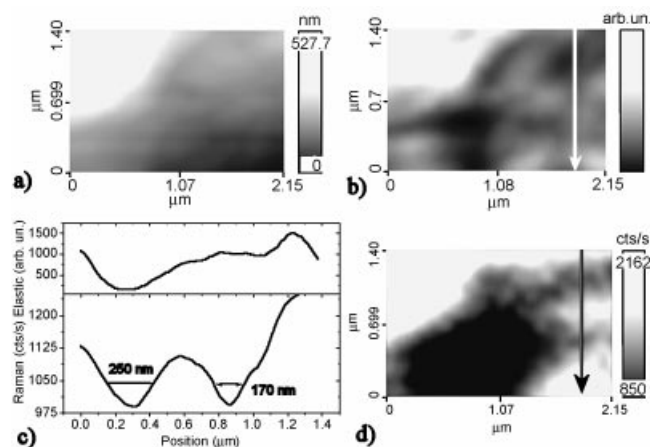


Fig. 9. The central picture shows a 3D rendering of the topography ( $10 \times 10\text{ }\mu\text{m}^2$ ) showing a doughnut-shaped structure  $\approx 5\text{ }\mu\text{m}$  wide, and  $\approx 500\text{ nm}$  high. The spectra acquired at different points allows us to assess the presence of neutral TCNQ in correspondence of that feature.

wide area ( $256 \times 103\text{ pts}$ ,  $\tau_{\text{INT}} = 100\text{ ms}$ ). We can observe the occurrence of topography structures having a doughnut shape with a diameter of several micrometres ( $\approx 5\text{ }\mu\text{m}$  on average), and heights ranging from 200 to 500 nm. In the Raman map only some of these doughnut-shaped features show a pronounced activity, the remaining background being induced by dark counts and, probably, unfiltered spurious laser light. The elastic scattering properties of such zones, reported previously in Gucciardi *et al.* (2002), appear similar to the Raman ones. This agreement would indeed be correct if TCNQ would occur inside these features, because of the smaller absorption of the TCNQ with respect to the surrounding CuTCNQ. Nevertheless, in order to exclude the presence of artefacts (in the sense summarized above in the text) and assess the genuine nature of the Raman signal recorded in the map, we carried out several spectra in different locations. The central picture of Fig. 9 is a 3D rendering of the topography signal acquired on a  $10 \times 10\text{ }\mu\text{m}^2$  area containing one of the above-mentioned reliefs. The Raman spectra depicted around ( $\tau_{\text{INT}} = 100\text{ ms}$ ) show that the relief is a TCNQ-rich structure and prove the genuine optical contrast of both the Raman and the elastic scattering maps. We can also observe that, at a distance from the feature, no correlation arises between the topography and the chemical properties of the surface. The spectrum carried out on the upper left corner of the topography map, where a valley can be observed, still shows the fingerprint of the TCNQ molecules. Conversely, the two other spectra carried out on the right-hand side of the map, where some surface features occur, are completely noisy proving that an almost complete CT transition has occurred in this region. Based on these observations, we can conclude that the sample



**Fig. 10.** Maps of the topography (a), elastic scattering (b), and Raman scattering at  $1453\text{ cm}^{-1}$  (d) simultaneously acquired on a portion  $2.15 \times 1.40\ \mu\text{m}^2$  wide. In the left upper corner the occurrence of a smaller doughnut-shaped feature is evident, surrounded by a zone showing localized TCNQ and CuTCNQ spots. The line profiles (c) of the elastic scattering (upper) and of Raman intensity (lower) allow us to exclude any fictitious cross-talk between the two signals and to assess a lateral resolution of  $\approx 170\text{ nm}$ .

morphology in the 'blue' zone is characterized by sparse doughnut-shaped structures, some of which are rich in TCNQ, whereas the surface among them is mainly composed of CuTCNQ, with some chemical inhomogeneity arising on submicrometre regions. This phenomenon is highlighted in Fig. 10 showing a zoom of the topography (Fig. 10a), the elastic scattering map (Fig. 10b), and the Raman map at  $1453\text{ cm}^{-1}$  (Fig. 10d), carried out on a  $2.15 \times 1.40\ \mu\text{m}^2$  area. Again part of a doughnut-shaped feature  $\approx 400\text{ nm}$  high is present on the upper left corner, appearing brighter both in the elastic scattering and in the Raman map, proving the presence of TCNQ therein. Besides, the occurrence of a dark CuTCNQ circular spot with dimensions in the micrometre range, can be seen in the Raman map. On the right-hand side is again present a region rich of TCNQ, with some copper contamination in between (darker). The Raman line profile (Fig. 10c, bottom line), drawn along the arrow depicted in the map, shows that the central TCNQ spot, with dimensions of  $\approx 350\text{ nm}$  (FWHM), is surrounded by two copper-rich zones having dimensions of 170 and 250 nm, responsible for a Raman intensity decrease of  $\approx 20\%$ . Again, there is a difference between the elastic and Raman scattering maps on subwavelength scales assessing that pure Raman contrast is reported in Fig. 10(d).

## Conclusions

In conclusion, we have shown the applications of a Raman-imaging NSOM set-up to two different samples based on TCNQ molecules. In the first sample the effects of surface damage

have been mapped, whereas the two chemical species occurring on the second sample have been discriminated by Raman means, and images of the different chemical morphologies taking place at different locations have been provided. Sub-diffraction resolution has been reported on both samples without the need for field enhancement effects. Because of the high Raman efficiency of the TCNQ molecules, the measurements were performed with unprecedented short integration times.

## Acknowledgement

Support by MURST within the Cluster C26, project no. 7 is greatly acknowledged.

## References

- Ayars, E.J., Hallen, H.D. & Jahncke, C.L. (2000) Electric field gradient effects in Raman spectroscopy. *Phys. Rev. Lett.* **85**, 4180–4183.
- Betzig, E., Finn, P. & Weiner, J.S. (1992) Combined shear force and near-field scanning optical microscopy. *Appl. Phys. Lett.* **60**, 2484–2486.
- Betzig, E., Trautman, J.K., Harris, T.D., Weiner, J.S. & Kostelak, R.L. (1991) Breaking the diffraction barrier: optical microscopy on a nanometric scale. *Science*, **251**, 1468–1471.
- Blochowitz, J., Pfeiffer, M., Fritz, T. & Leo, K. (1998) Low voltage organic light emitting diodes featuring doped phtalocyanine as hole transport material. *Appl. Phys. Lett.* **73**, 729–731.
- Deckert, V., Ziesel, D., Zenobi, R. & Vo-Dinh, T. (1998) Near-field surface-enhanced Raman imaging of dye-labeled DNA with 100-nm resolution. *Anal. Chem.* **70**, 2646–2650.
- Emory, S.R. & Nie, S. (1997) Near-field surface-enhanced Raman spectroscopy on single silver nanoparticles. *Anal. Chem.* **69**, 2631–2635.
- Futamata, M. & Bruckbauer, A. (2001) ATR-SNOM-Raman spectroscopy. *Chem. Phys. Lett.* **341**, 425–460.
- Gao, W. & Kahn, A. (2001) Controlled *p*-doping of zinc phtalocyanine by coevaporation with tetrafluorotetracyanoquinodimethane: a direct and inverse photoemission study. *Appl. Phys. Lett.* **79**, 4040–4042.
- Graja, A. (1997) *Spectroscopy of Materials for Molecular Electronics*. Scientific Publishers, Poznan.
- Grausem, J., Humbert, B., Burneau, A. & Oswald, J. (1997) Subwavelength Raman spectroscopy. *Appl. Phys. Lett.* **70**, 1671–1673.
- Gucciardi, P.G. & Colocci, M. (2001) Different contrast mechanisms induced by topography artefacts in near-field optical microscopy. *Appl. Phys. Lett.* **79**, 1543–1545.
- Gucciardi, P.G., Labardi, M., Gennai, S., Lazzeri, F. & Allegrini, M. (1997) A versatile scanning near-field optical microscope for material science applications. *Rev. Sci. Instrum.* **68**, 3088–3092.
- Gucciardi, P.G., Trusso, S., Vasi, C., Patanè, S. & Allegrini, M. (2002) Nano-Raman imaging of CuTCNQ clusters in TCNQ thin films by scanning near-field optical microscopy. *Phys. Chem. Chem. Phys.* **4**, 2747–2753.
- Hayazawa, N., Inouye, Y., Sekkat, Z. & Kawata, S. (2000) Metallized tip amplification of near-field Raman scattering. *Opt. Commun.* **183**, 333–336.
- Hayazawa, N., Inouye, Y., Sekkat, Z. & Kawata, S. (2001) Near-field Raman scattering enhanced by a metallized tip. *Chem. Phys. Lett.* **335**, 369–374.

- Hecht, B., Bielefeldt, H., Inouye, Y., Pohl, D.W. & Novotny, L. (1997) Facts and artifacts in near-field optical microscopy. *J. Appl. Phys.* **81**, 2492–2498.
- Higo, M., Lu, X., Mazur, U. & Hipps, K.W. (2001) Atomic force microscopy observation of the morphology of TCNQ deposited from solution onto the atomically smooth native oxide surface of Al(111) films. *Thin Solid Films*, **384**, 90–101.
- Hua, Z.Y. & Chen, G.R. (1992) A new material for optical, electrical and electronic thin film materials. *Vacuum*, **43**, 1019.
- Jahncke, C.L., Hallen, H.D. & Paesler, M.A. (1996) Nano-Raman spectroscopy and imaging with near-field scanning optical microscope. *J. Raman Spectrosc.* **27**, 579–586.
- Jahncke, C.L., Paesler, M.A. & Hallen, H.D. (1995) Raman imaging with near-field scanning optical microscopy. *Appl. Phys. Lett.* **67**, 2483–2485.
- Karrai, K. & Grober, R.D. (1995) Piezoelectric tip-sample distance control for near-field optical microscopes. *Appl. Phys. Lett.* **66**, 1842–1844.
- Lewis, A., Isaacson, M., Harootunian, A. & Murry, A. (1984) Development of a 500 Å spatial resolution light microscope. *Ultramicroscopy*, **13**, 227–232.
- Liu, S.-G., Liu, Y.-Q., Wu, P.-J., Zhu, D.-B., Tian, H. & Chen, K.-C. (1996) Characterisation and electrical property of molten-grown CuTCNQ film material. *Thin Solid Films*, **289**, 300–305.
- Pohl, D.W., Denk, W. & Lanz, M. (1984) Optical stethoscopy: image recording with resolution  $\lambda/20$ . *Appl. Phys. Lett.* **44**, 651–653.
- Smith, D.A., Webster, S., Ayad, M., Evans, S.D., Fogherty, D. & Batchelder, D. (1995) Development of a scanning near-field optical probe for localised Raman spectroscopy. *Ultramicroscopy*, **61**, 247–252.
- Stöckle, R., Fokas, C., Deckert, V., Zenobi, R., Sick, B., Hecht, B. & Wild, U.P. (1999) High-quality near-field optical probes by tube etching. *Appl. Phys. Lett.* **75**, 160–162.
- Stöckle, R.M., Suh, Y.D., Deckert, V. & Zenobi, R. (2000) Nanoscale chemical analysis by tip-enhanced Raman spectroscopy. *Chem. Phys. Lett.* **318**, 131–136.
- Toledo-Crow, R., Yang, P.C., Chen, Y. & Vaez-Iravani, M. (1992) Near-field differential scanning optical microscope with atomic force regulation. *Appl. Phys. Lett.* **60**, 2957–2959.
- Tsai, D.P., Othonos, A., Moskovits, M. & Uttamchandani, D. (1994) Raman spectroscopy using a fiber optic probe with subwavelength aperture. *Appl. Phys. Lett.* **64**, 1768–1770.
- Webster, S., Batchelder, D.N. & Smith, D.A. (1998) Submicron resolution measurement of stress in silicon by near-field Raman spectroscopy. *Appl. Phys. Lett.* **72**, 1478–1480.
- Ziesel, D., Deckert, V., Zenobi, R. & Vo-Dinh, T. (1998) Near-field surface-enhanced Raman spectroscopy of dye molecules adsorbed on silver island films. *Chem. Phys. Lett.* **283**, 381–384.